ELSEVIER

Physica D 96 (1996) 259–271

PHYSICA D

Optical pattern formation in a Kerr-like medium with feedback

P.L. Ramazza *, E. Pampaloni, S. Residori, F.T. Arecchi

Istituto Nazionale di Ottica, Largo E. Fermi 6, Firenze, Italy

Abstract

We present a series of experiments on pattern formation in an optical system including a Liquid Crystal Light Valve (LCLV), that with good approximation behaves like a Kerr medium, inserted in a feedback loop. We discuss the physical origin of the length scales and of the various symmetries that are observed close to the threshold for pattern formation.

PACS: 42.50.N; 82.40.C; 42.79.K

Keywords: Pattern formation; Nonlinear optics; Symmetries; Liquid crystal light valves

1. Introduction

Nonlinear optical set-ups formed by a Kerr-like medium with feedback have become a popular subject of study for two-dimensional (2D) transverse pattern formation [1–8]. Here we present experiments on pattern formation and competition in a system formed by a Liquid Crystal Light Valve (LCLV) with optical feedback. As a first approximation, the LCLV can be considered as a defocusing Kerr-like medium [9].

The pattern forming phenomena discussed here are based on the conversion of the phase fluctuations induced on an optical beam by the LCLV into intensity fluctuations. This occurs via diffraction of the beam [2]. When the diffracted output beam is sent onto the rear face of the LCLV the feedback loop is closed and this can give rise to dynamical instabilities.

It is worth emphasizing three main features of the patterns spontaneously formed from a homogeneous state, namely length scales, shape and dynamical behavior.

The nature of the observed phenomena is strictly related on one side to the Kerr nature of the nonlinearity and to the presence of diffusion in the medium, and on the other side to the geometrical constraints that are imposed in the feedback loop. The experiments show that the length scale of the patterns is determined by the joint contribution of diffractive and diffusive phenomena occurring in the system.

As for the shapes of the structures that form, these can be determined by different factors. In the case in which the feedback loop is simply a propagation path, it is the quadratic nature of the Kerr nonlinearity that dominates, leading to the formation of hexagons or rolls [2–5]. When a limiting aperture of size comparable to the intrinsic length of the pattern is added within the feedback loop, the role of the transverse boundary conditions overwhelms the other effects, resulting in the formation of polygon-like structures [6,8]. In this case, for increasing input intensity, polygon rotation or alternation of different polygons in time is observed.

For large apertures, if a nonlocal interaction of the signal with itself is introduced in the feedback loop via

* Corresponding author.

PII S0167-2789(96)00026-7

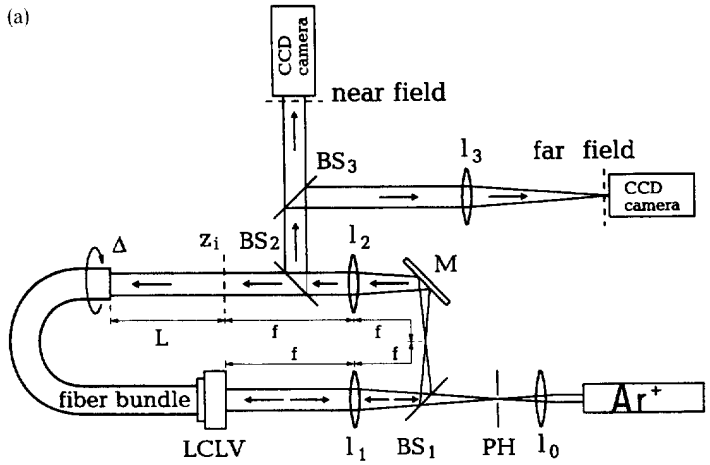

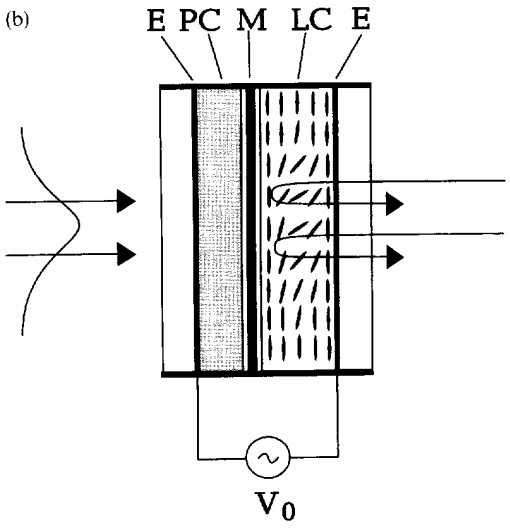

Fig. 1. (a) Experimental set-up; l_i = lens, M = mirror, BS_i = beam splitters, PH = pinhole, L = free propagation length, Δ = feedback rotation angle. (b) Liquid Crystal Light Valve (LCLV): LC = liquid crystal layer, M = mirror, PC = photoconductor layer, E = transparent electrodes, V_0 = applied AC voltage. The liquid crystal molecules re-orient accordingly to the write intensity incident on the PC.

a rotation in the transverse plane, new classes of symmetries arise in the patterns, corresponding to crystalline or quasi-crystalline structures [7]. For this case linear stability analysis of the problem gives case rotation dependent selection rules for the wavelength of the excited patterns. The validity of these rules is confirmed by the experiments.

2. Experimental set-up

The system used in the experiments consists of a LCLV inserted in an optical feedback loop as shown in Fig. 1(a). A drawing of the LCLV is shown in Fig. 1(b). This device consists of a nematic liquid crystal cell, a dielectric mirror and a photoconductive layer. A supply voltage V_0 is applied through transparent electrodes to these three elements in series. The nematic liquid crystal layer displays a birefringence whose amount is a monotonically decreasing function of the voltage V_{LC} across it [10]. Since the liquid crystal layer and the photoconductor are placed in series, the fraction that V_{LC} is of the supply voltage V_0 will increase when the illumination incident on the photoconductive layer increases. It follows that a writing beam impinging on the rear side of the LCLV induces a variation in the extraordinary index of refraction of the liquid crystals. This variation is of negative sign and in first approximation proportional to the writing intensity, so that the LCLV can be considered as a defocusing Kerr medium.

In our experimental set-up a beam from an Ar^+ laser operating at 514 nm is spatially filtered and expanded by means of the telescope system formed by lenses l_0 and l_1 and pinhole PH. The resulting plane wave, polarized along the extraordinary axis of the liquid crystal, is sent on the front face of the LCLV. The wave reflected by the LCLV acquires a spatial phase

modulation, which is determined by the distribution of the extraordinary index of refraction n in the liquid crystal layer. The front plane of the LCLV is imaged onto plane z_i by means of lenses l_1 and l_2. Along the image forming path, a fraction of the beam is extracted at beam splitter BS_2 and used for detection of the near- and far-field signal. From plane z_i to the input plane z_2 of the fiber bundle the wave undergoes a free propagation path of length L. At plane z_2 the diffracted wave enters an optical fiber bundle, that just relays the intensity distribution from its input to its output plane. The output plane of the fiber bundle is in contact with the rear face of the LCLV.

The origin of pattern formation in a system of this kind lies in the following mechanism [2]. Perturbations of the index of refraction n in the liquid crystal layer induce a phase modulation in the reflected beam. This phase modulation is converted into amplitude modulation by diffractive propagation along L. The light intensity reaching the rear side of the LCLV provides via the Kerr effect a feedback on the perturbations of n. The system is therefore governed by a diffusive equation, containing the feedback intensity I_{FB} as a source term [1]:

$$\frac{\partial n(\boldsymbol{r},t)}{\partial t} + n + l_D^2 \nabla_\perp^2 n = \chi I_{FB}(\boldsymbol{r},t), \tag{1}$$

where l_D is diffusion length in the liquid crystal layer, $\nabla_\perp^2$ denotes the transverse Laplacian operator, and χ gives the sign and the strength of the Kerr nonlinearity. Eq. (1) must be supplemented with a relation expressing the dependence of I_{FB} on n. This relation reads [2]:

$$I_{FB} = f\left(I_0 \left| e^{-i(L\nabla_\perp^2/2k_0)} e^{-in(\boldsymbol{r},t)} \right|^2\right), \tag{2}$$

where I_0 is the input intensity. The term inside the parentheses is the solution of the free propagation equation along L, and the function $f(I)$ represents the transformation of the light distribution from plane z_2 to the rear plane of the LCLV. In our experiment we investigate the pattern formation in the system for the case in which the transformation $f(I)$, the identity transformation, a pupil function, or a rotation are in the transverse plane.

3. Hexagons and rolls formation for infinite transverse boundary

Let us consider the simplest experimental configuration, in which the function $f(I)$ appearing in Eq. (2) is the identity. Linear stability analysis of Eq. (1) gives the marginal stability curve [2]:

$$\chi I_0 = \frac{1 + l_D^2 q^2}{\sin(q^2 L/2k_0)} \tag{3}$$

for the Fourier component of n at spatial frequency q. Plots of the curves (3) are given in Fig. 2 for two different values of l_D. It is seen that diffusion of the excitation in the LC layer tends to raise the instability threshold for high q modes, while the diffractive contributions determine the minima (maxima for $\chi < 0$) of the curves. These extrema occur for $q^2 L/2k_0 = N(\pi/2)$, with N an odd integer, and give the location of the most unstable modes.

The half-planes above and below the horizontal axis in Fig. 2 represent the situation, respectively, for the case of focusing and defocusing Kerr medium. The results of the linear stability analysis provide information only on the scale of the unstable patterns, and not on their shape. In order to gain information about this, nonlinear analysis of Eq. (1) is required. It has been shown [2] that the system can be suitably described by expanding the index perturbation n in the sum of three Fourier components having the same wave number, and oriented at 120° with respect to the other:

$$n = n_0 + \sum_{i=1}^{3} A_i e^{i\boldsymbol{k}_i \cdot \boldsymbol{r}}, \quad \sum_{1}^{3} \boldsymbol{k}_i = 0. \tag{4}$$

This leads to the coupled nonlinear equations:

$$\begin{aligned}
\frac{dA_1}{dt} &= \mu A_1 + \alpha_i A_2^* A_3^* \\
&\quad -\beta(|A_2|^2 + |A_3|^2)A_1 - \gamma |A_1|^2 A_1, \\
\frac{dA_2}{dt} &= \mu A_2 + \alpha_i A_1^* A_3^* \\
&\quad -\beta(|A_1|^2 + |A_3|^2)A_2 - \gamma |A_2|^2 A_2, \\
\frac{dA_3}{dt} &= \mu A_3 + \alpha_i A_1^* A_3^* \\
&\quad -\beta(|A_1|^2 + |A_2|^2)A_3 - \gamma |A_3|^2 A_3.
\end{aligned} \tag{5}$$

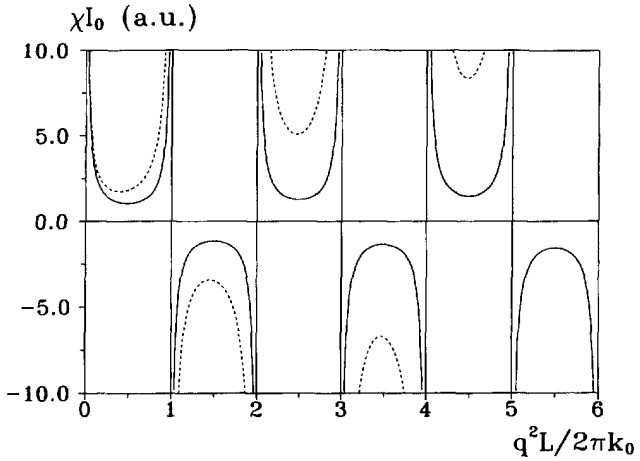

Fig. 2. Marginal stability curves corresponding to Eq. (3), for $L = 30$ cm, $k_0 \equiv 2\pi/\lambda$, $\lambda = 514$ nm. Solid line: $l_D = 20$ μm; dashed line: $l_D = 80$ μm.

These equations admit two stationary solutions, namely:

$$A_1 = 0, \quad A_2 = A_3 \neq 0, \tag{6}$$

corresponding to rolls or

$$A_1 = A_2 = A_3 \neq 0 \tag{7}$$

corresponding to hexagons. For the parameters proper for our system, only the hexagons are stable [2].

In our experiment the free propagation length L is of the order of 10 cm. This leads to a value of the wavelength $\Lambda = 2\pi/q$ for the first excited mode of the order of some hundreds of microns. Since the transverse extension of the beam in the system is $\simeq 5$ mm, we expect that the experimental result be well described by the infinite transverse boundary model described above. Fig. 3 displays a typical image of the near-field pattern, formed by a highly regular hexagonal tiling. The perfect regularity of the pattern persists until the transverse size of the system becomes too large, or the level of excitation of the system, that is controlled by varying I_0, is increased far above threshold. In both cases some defects in the hexagonal pattern are observed in the form of penta–hepta pairs.

Let us now investigate the consequences of breaking the rotational symmetry of the system. As a first step, consider what happens when a rotation of π is introduced in the feedback loop. In this case the continuous rotational symmetry of the system is broken, but only in a weak way, in the sense that any pixel on the wavefront is now mapped onto itself not after one round trip, but after two round trips across the cavity. The system can therefore be seen as the combination of two coupled subsystems, corresponding to the two halves of the LCLV. Equation similar to (5) can still be written [5] for the two coupled subsystems, and the analysis of the solutions shows that now only the roll pattern is stable. Furthermore, the scale of the excited

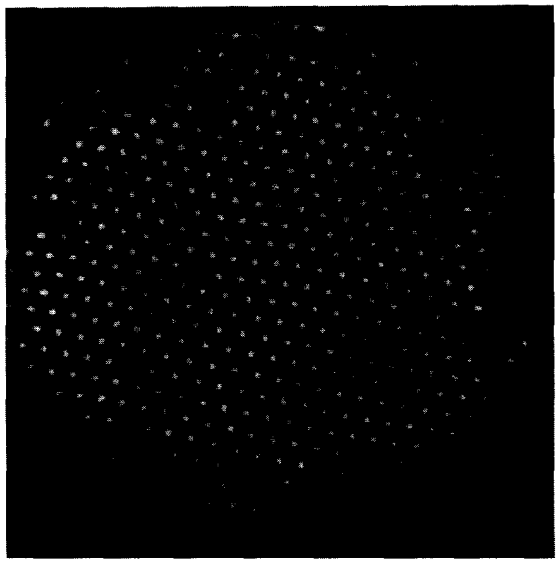

Fig. 3. Hexagonal pattern in the case of 0° rotation.

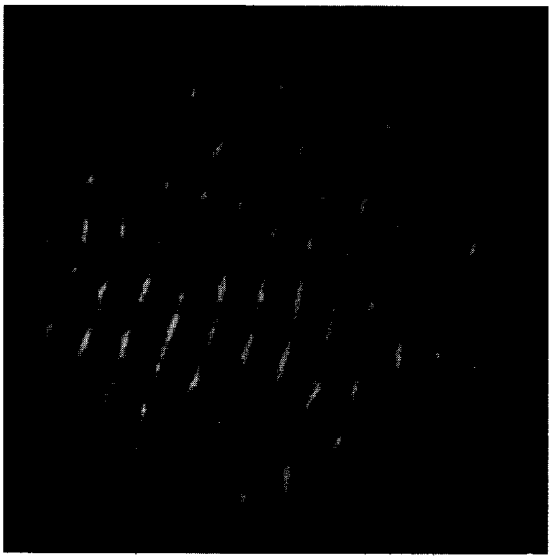

Fig. 4. Roll pattern in the case of 180° rotation.

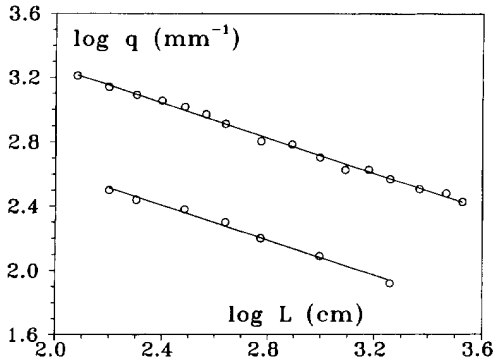

Fig. 5. Measured pattern wave number q as a function of the propagation distance L. Upper curve: $\Delta = 0°$ (hexagon pattern); lower curve: $\Delta = 180°$ (roll pattern). Straight lines are best fit with $q \sim L^{-0.5}$.

pattern is in this case given by $q = \sqrt{\pi k_0/L}$, and not by $q = \sqrt{3\pi k_0/L}$ as in the zero rotation case. Fig. 4 shows a typical near-field pattern obtained in these conditions. In Fig. 5 we show the dependence of the excited wave number q vs. the free propagation length L for the cases of 0 and π rotation. It is seen here that the predicted diffractive scaling $q \simeq 1/\sqrt{L}$ is in excellent agreement with the experimental results.

A strong breaking of the rotational symmetry is then obtained by introducing an input intensity gradient along the horizontal direction. The equations describing the evolution of the signal on the two halves of the system are now coupled by two parameters $p = (p_1 + p_2)/2$ and $\delta = (p_1 - p_2)/2p$, p_1 and p_2 being the normalized intensity impinging on each half [5,11]. Plots of the far-field patterns obtained in this case are shown in Fig. 6, together with the corresponding spatial profiles of output intensity. The most striking effect of the strong symmetry breaking introduced is the restoration of the hexagonal symmetry of the pattern. This result can be obtained by linear stability analyses of the roll and hexagon solutions [5], whose results are shown in Fig. 7. For μ close to threshold, a subcritical bifurcation of hexagonal pattern is expected. This solution looses its stability and is replaced by rolls at high values of μ, that are not possible to reach by using our present experimental set-up.

4. Polygon formation for small transverse boundary

The role of the transverse boundary condition in affecting the pattern formation in a system equivalent to ours, has been theoretically investigated in [8]. The main results of that analysis, based on symmetry arguments, are the possibility of primary pattern forming bifurcations leading to formation of polygons, and of secondary bifurcations resulting either in single polygon rotation or in alternation between different polygons in the course of time. From an experimental point of view, we are able to vary the transverse boundary condition of the system by placing a variable aperture in the plane z_i of Fig. 1. This corresponds to a choice of the function $f(I)$ appearing in (2) of the form:

$$f(I) = \begin{cases} 1 & \text{for } r < r_0, \\ 0 & \text{for } r > r_0, \end{cases} \tag{8}$$

where r is the radial coordinate in z_i plane, and r_0 is the radius of the limiting aperture.

In Fig. 8 we present pictures of the near-field patterns observed for various values of r_0, keeping the input intensity I_0 close to the pattern formation threshold. Formation of stationary polygons with group symmetry D_l is observed as expected. The

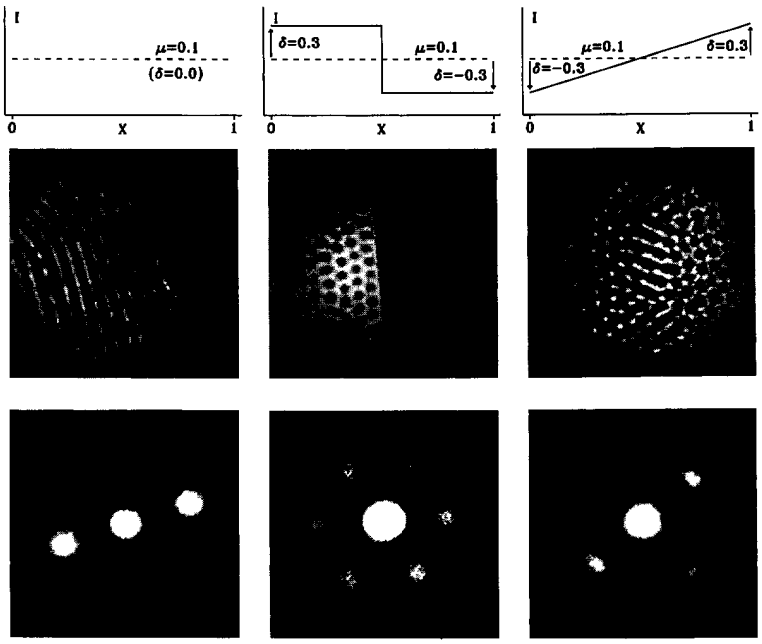

Fig. 6. Experimentally observed patterns: rolls, hexagons, hexagons + rolls (upper) and corresponding far-field patterns (lower). On the top we report for each of the three situations a diagram of the feedback intensity I versus transverse position (normalized between 0 and 1). We calibrate the average intensity in μ units and the offset in δ units, with reference to the control parameters used in the stability diagrams of Fig. 7.

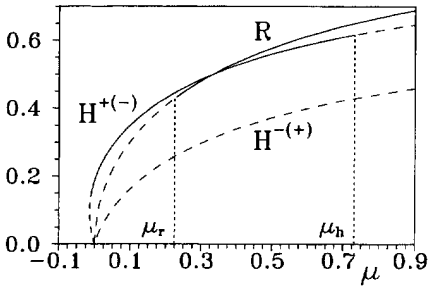

Fig. 7. Bifurcation diagram for $\delta = 0.3$; R is the amplitude of the roll solution, $H^{+(-)}$ is the amplitude of the positive (negative) hexagons solution. Solid lines correspond to stable solutions; dashed lines to unstable ones.

index l, indicating the number of axes around which a polygon is rotationally invariant, is an increasing function of r_0. Notice that, since the system is kept close to threshold, the spacing among the bright spots is nearly the same for all the values of r_0.

Fig. 9 shows the far-field intensity corresponding to near-field polygons with $l = 3, 2$ and 6. This allows visualization of the spatial power spectra of the polygons. Notice that the spectra for $l = 2$ and 3 differ only slightly from the one for $l = 6$. Indeed, polygons with $l = 2$ and 3 are equivalent to parts of an underlying hexagonal structure, whose existence is limited in space by the presence of the aperture. A completely different situation takes place for $l = 5$ and 7. The power spectra relative to these cases are shown in Fig. 10. This difference is due to the fact that the polygons with $l = 5$ and 7, namely pentagons and heptagons, cannot arrange themselves in a hexagonal like structure covering the plane.

It is worth noticing that, in conditions of perfect rotational symmetry, polygons with all the possible azimuthal orientations have the same instability threshold. This kind of degeneracy is lifted by the presence in the experimental system of some imperfections, occurring mainly under the form of optical aberrations (e.g. astigmatism). For this reason a preferred orientation of the polygons exists close to the pattern formation threshold.

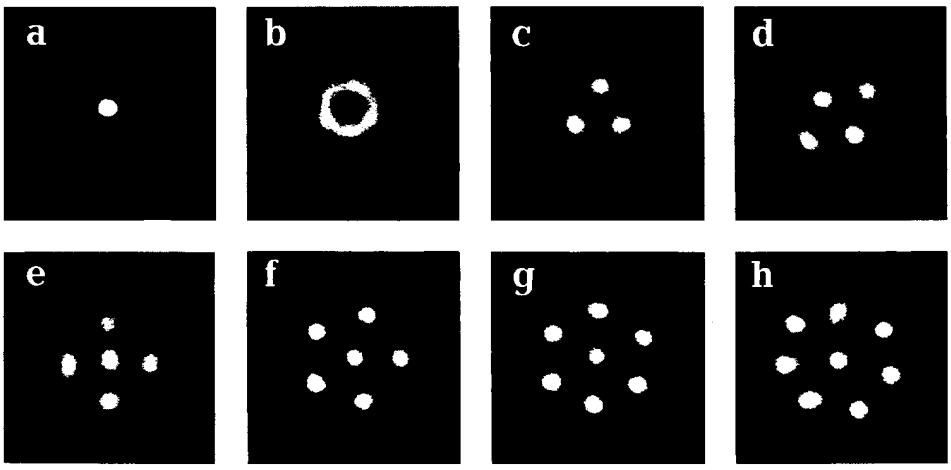

Fig. 8. Near-field images of the patterns observed for an increasing aperture: (a) for $d = 1$ mm only a single spot is allowed by the aperture; (b) for $d = 1.1$ mm an annulus goes above threshold; (c)–(h): D_l symmetries observed, namely, (c) $l = 3$ ($d = 1.2$ mm), (d) $l = 2$ ($d = 1.4$ mm), (e) $l = 4$ ($d = 1.5$ mm), (f) $l = 5$ ($d = 1.7$ mm), (g) $l = 6$ ($d = 1.9$ mm), (h) $l = 7$ ($d = 2.2$ mm).

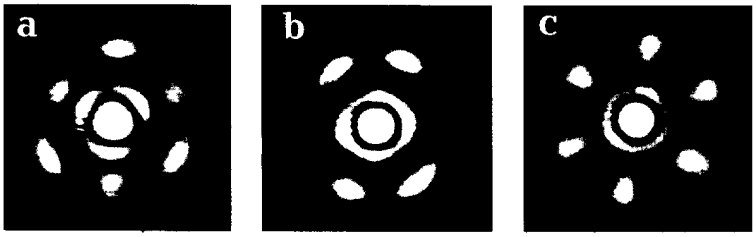

Fig. 9. Far-field images of patterns with D_l symmetries: (a) $l = 3$, (b) $l = 2$, (c) $l = 6$.

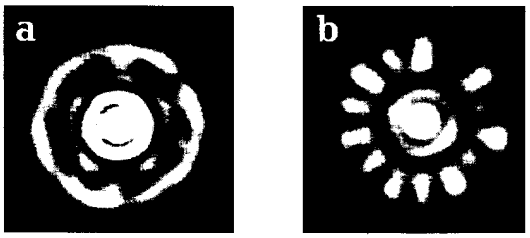

Fig. 10. Far-field images of patterns with D_l symmetries: (a) $l = 5$, (b) $l = 7$.

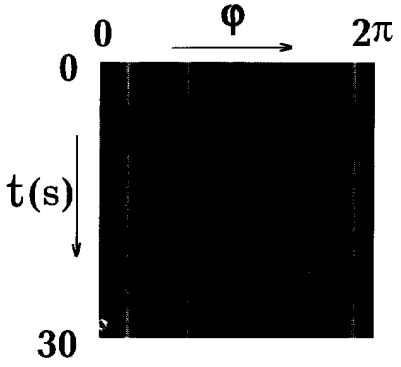

Fig. 11. Space–time diagram of a pentagonal pattern whose orientation fluctuates in time. The data acquisition line, as a function of the azimuthal angle φ, is plotted versus time t. (See Fig. 12 for comparison with a rotating pattern situation.)

If the input intensity I_0 is increased slightly above threshold the azimuthal degeneracy can be at least partially restored. As a consequence, fluctuations in time of the polygon orientation are observed, as shown in Fig. 11.

When I_0 is further increased, secondary bifurcations of the patterns occur. Under these circumstances, rotation in time of a single polygon can be observed. An example of this situation is shown in Fig. 12. Here the rotation of the pentagon shown in Fig. 12(a) is revealed by looking at the time evolution of the gray

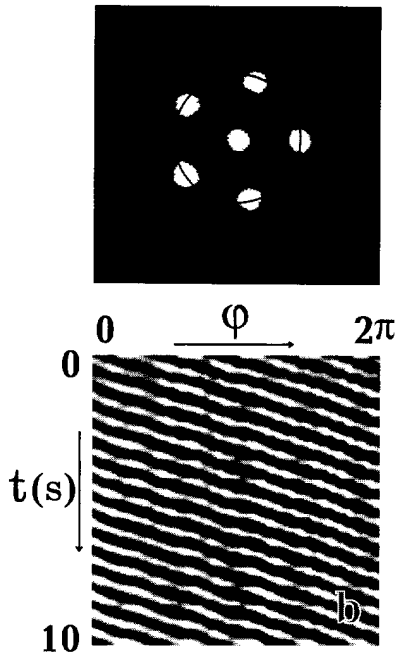

Fig. 12. (a) Rotating pattern with D_5 symmetry, the gray circle corresponds to the data acquisition line; (b) space–time diagram of the rotating pattern: the data acquisition line, as a function of the azimuthal angle φ, is plotted versus time t.

circle. The space–time plot obtained from this signal, shown in Fig. 12(b), reveals the very regular rotational dynamics of the pentagon.

Time alternation between different polygons is also possible. In order to quantitatively characterize this phenomenon, we proceed in the following way. We acquire in the course of time a series of pictures of the near-field signal, separated in time by 0.2 s. Digital thresholding of these images results in binarization of the signal. Since any bright spot belonging to the polygons has approximately the same area, it is possible to determine which polygon is present at any time by just dividing the total bright area of a binarized image by the area of a single spot. The result of this procedure is shown in Fig. 13(a). Time alternation between a pentagon and a hexagon is observed in this case. The power spectrum of the measured time series, shown in Fig. 13(b), clearly displays the periodic nature of this time alternation.

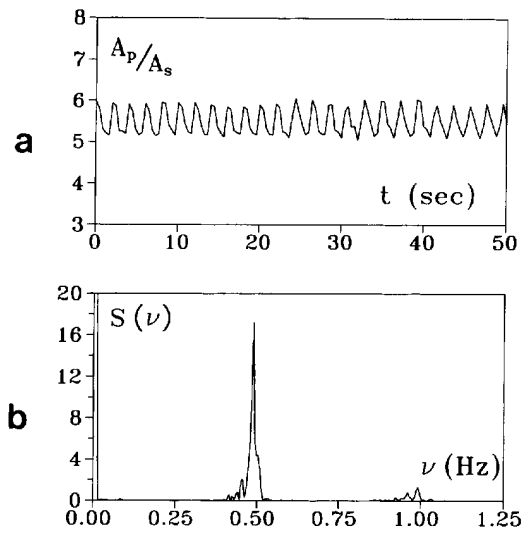

Fig. 13. Periodic alternation between $l = 5$ and $l = 6$ patterns: (a) time evolution of the measured pattern area A_p normalized to the average single spot area A_s; (b) power spectrum of the signal.

5. The role of nonlocal interaction: Crystals and quasi-crystals

In this section we describe the effect of a nonlocal interaction on the pattern formation phenomena occurring in our system. Nonlocality is introduced by means of rotation of the signal in the feedback loop obtained by rotating the fiber bundle shown in Fig. 1. This corresponds to a choice of the function $f(I)$ appearing in (2) of the form

$$f(I(r,\theta)) = I(r,\theta+\Delta), \tag{9}$$

where (r,θ) are polar coordinates in the plane, and Δ is the rotation angle introduced. In the experiments here presented, $\Delta = 2\pi/N$, with N integer. We are therefore in condition of infinite transverse boundary, but the rotational symmetry of the system is now only discrete. Furthermore, the translational symmetry of the system is broken by the existence of the rotation term.

Under these conditions, the set of crystalline structures for which a perfect tiling of the transverse plane is possible is strongly limited. A crystal is indeed defined as a structure characterized by an elementary cell that replicates identical to itself, filling uniformly the

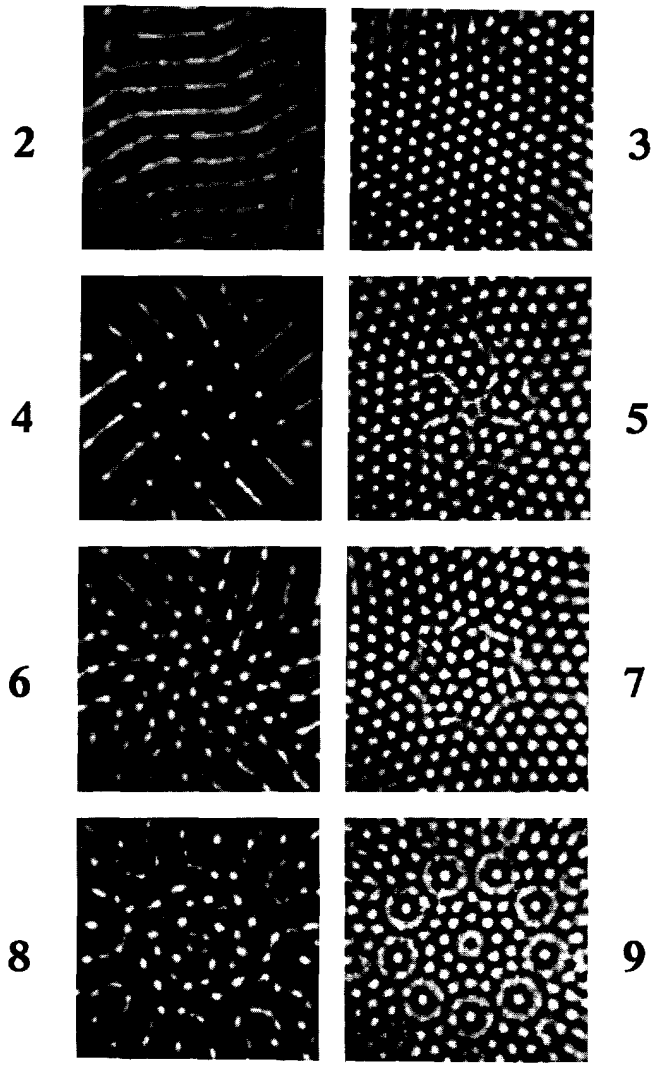

Fig. 14. Near-field patterns observed for feedback rotation angles $\Delta = 2\pi/N$. The N values are indicated close to each frame.

plane and giving rise to a pattern displaying long range translational order. When the additional constraint of discrete rotational symmetry is imposed, crystals can only form having an elementary cell formed by rolls, hexagons, squares or equilateral triangles. These structures display respectively 2-, 3-, 4- and 6-fold rotational symmetry plus translational symmetry. Hence, it is to be expected that, for N different from 2, 3, 4 and 6, structures different from crystals will be formed in our system.

Pictures of the near-field patterns obtained experimentally for various values of N are shown in Fig. 14. The corresponding far-field patterns are shown in Fig. 15. As expected, the near-field patterns are of crystalline type for $N = 2, 3, 4$ and 6. For all the other values of N, the structures display long range orientational order, quasi-periodical translational order and self-similarity. These properties correspond to the definition of quasi-crystals, that have recently been investigated both from an experimental [12]

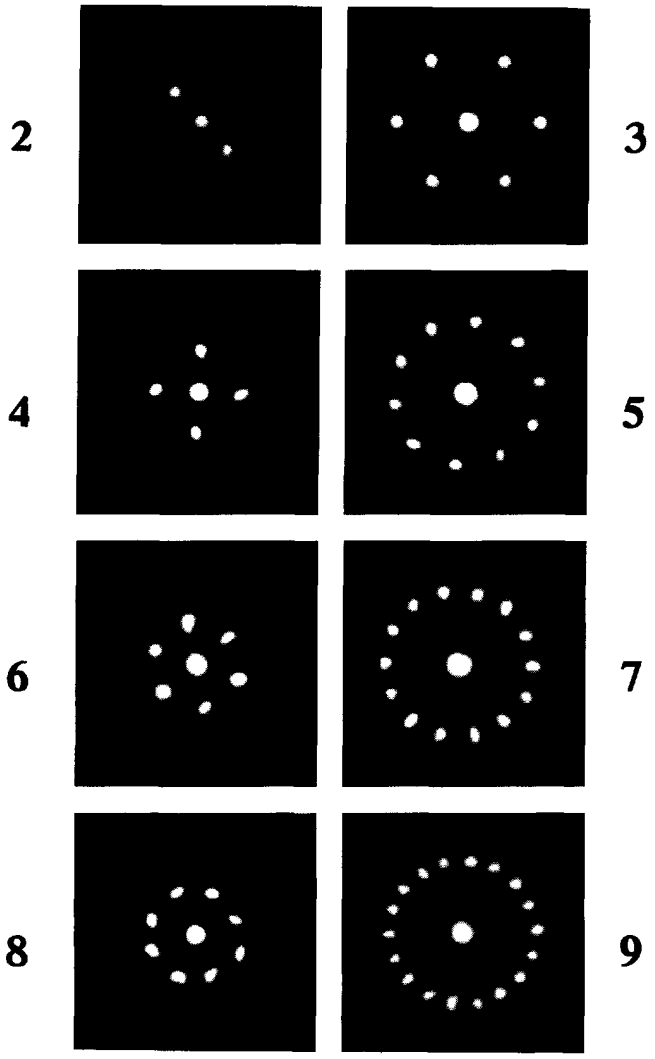

Fig. 15. Far-field patterns observed for feedback rotation angles $\Delta = 2\pi/N$. The N values are indicated close to each frame. All frames correspond to the same magnification, thus the rings with N even and those with N odd are, respectively, proportional to q_{I} and q_{II}.

and from a theoretical [13] points of view. Quasi-periodical translational order in the far-field patterns is revealed by the fact that, along any diameter in the Fourier plane, the ratio of the projection of two different wave vectors is irrational. Self-similarity is also visible in the far-field patterns, but only when the level of I_0 is increased well above the threshold value. Pictures relative to this situation are shown in Fig. 16.

From an experimental point of view, the condition $\Delta = 2\pi/N$ can be set only approximately. Actually we observe that crystalline and quasi-crystalline structures exist for a range of Δ of the order of some tenths of degree around the ideal value. When Δ is set to an intermediate value between $2\pi/N_1$ and $2\pi/N_2$, with N_1 and N_2 successive integers, more complicated patterns appear. These last ones usually display azimuthal rotation in time

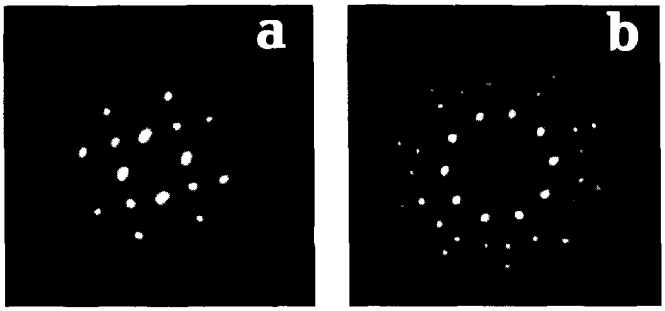

Fig. 16. Far-field patterns in the nonlinear regime (input intensity five times above threshold). To avoid saturation, the central region has been filtered out. In case (a) ($N = 4$) there is evidence of nonlinear peaks arranged on a periodic lattice. In case (b) ($N = 5$) secondary and tertiary peaks correspond to wave numbers close respectively to $\sqrt{7/3}$ and $\sqrt{11/3}$ times that (q_{II}) of the main peaks.

with large scale spiral-like structure, as reported in [1].

Looking both at the near and at the far-field patterns, it appears evident that the introduction of the nonlocal interaction influences not only the symmetry of the structures but also their scale. It is clear indeed that the Fourier bands excited for N even and for N odd are different. This phenomenon can be explained by a linear stability analysis of the problem. Let us start from Eqs. (1) and (2) of Section 2, and suppose that the homogeneous solution is perturbed by a phase modulation of wave vector $\boldsymbol{q}$ and that the feedback rotation by an angle $\Delta = 2\pi/N$ excites N vectors with the same length in N directions spaced by the angle Δ. Following Ref. [14], the phase perturbation can be expanded as $n = \sum_{j=1}^{N} a_j \cos \boldsymbol{q}_j \cdot \boldsymbol{r}$. The $\boldsymbol{q}$ vectors are related by the rotation operator in such a way that $R\boldsymbol{q}_j = \boldsymbol{q}_{j+1}$. With this expansion, propagation of the field over a distance L gives rise to the following feedback intensity

$$I_{FB}(L, \boldsymbol{r}, t) = I_0\left(1 + \sin\left(\frac{q^2 L}{2k_0}\right) \sum_{j=1}^{N} a_j \cos \boldsymbol{q}_j \cdot \boldsymbol{r}\right). \tag{10}$$

Substituting this expression into Eq. (1), we evaluate the eigenvalues λ_j of the perturbation vector $(a_1, a_2, \ldots, a_N)$ as $\lambda_j = -(1 + l_D^2 q^2) + \chi I_0 \sin q^2 L/2k_0 [e^{iN\pi}]_j^{1/N}$, where $[\ ]_j^{1/N}$ denotes the jth N_{th} root of unity. By selecting the eigenvalues with maximal real part, we derive two marginal stability curves

Branches I:

$$\chi I_{th} = \begin{cases} \dfrac{1 + l_D^2 q^2}{\sin(q^2 L/2k_0)} & \text{for } N \text{ even}, \\ \dfrac{1 + l_D^2 q^2}{\cos(\Delta/2)\sin(q^2 L/2k_0)} & \text{for } N \text{ odd}. \end{cases} \tag{11}$$

Branches II:

$$\chi I_{th} = \frac{1 + l_D^2 q^2}{\sin(q^2 L/2k_0)} \quad \text{for } N \text{ even or odd}. \tag{12}$$

The positive branches of these two curve give the value I_{th} of the input intensity I_0 necessary to excite an instability with a spatial frequency q. In the diffractive limit, $l_D^2 \ll \lambda L$, all branches have their minima at $q^2 L/2k_0 = (2n + 1)\pi/2$ with $n = 0, 2, \ldots$ (even integer) for branches I and $n = 1, 3, \ldots$ (odd integer) for branches II, so that, with respect to the first critical wave number $q_I = \sqrt{\pi k_0/L}$, the next is located at $q_{II} = \sqrt{3} q_I$ and the higher ones at $\sqrt{5} q_I$, $\sqrt{7} q_I, \ldots$ Close to threshold, only the first two branches of I and II (reported in Fig. 17(a)) are involved in the wave number selection process since they have the lowest minima. Furthermore, for N odd, branch I depends on N through Δ, hence its minimum can be above or below that of branch II. At threshold, the lowest local minimum determines the excited mode.

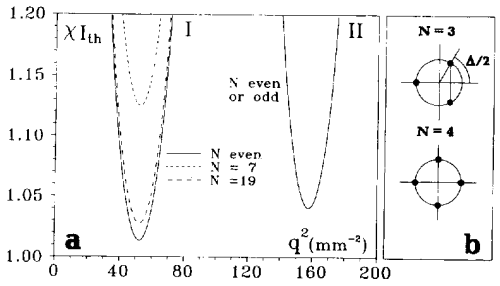

Fig. 17. (a) Marginal stability curves evaluated for $L = 75$ cm and $l_D = 15.5$ μm. The first branch has the lowest threshold for any N if N is even and also for N odd if N is large. For N odd and small the second branch has a lower threshold. (b) The N roots of unity in the complex plane, for $N = 3$ and 4. For $N = 3$ it is easy to see the enhancement factor $1/\cos(\Delta/2)$ found in Eq. (4) for N odd.

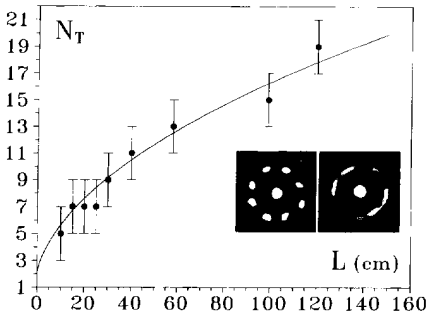

Fig. 18. Measured values N_T as a function of the free propagation length L. The best fit line corresponds to $l_D = 15.5$ μm. In the inset the far-field patterns, for $L = 30$ cm and $N = 8$ (left) and 9 (right), show that, at variance with the previous figure, here the ring has the same radius q_I in both cases, as expected from the N_T curve.

Comparing the magnitude of the real parts of the two unstable eigenvalues, we find that for N even the excited mode is always the one with q_I, independently of N. On the other hand, for N odd branch I has an enhancement factor $1/\cos(\Delta/2)$ (see Eq. (11)) which is larger for lower N, as shown for $N = 3$ in Fig. 17(b), and hence branch II is favored, whereas for high values of N there exists a pair of eigenvalues closest to the real axis, for which branch I can still have the lower threshold. For intermediate N the minima of branch I and II can be aligned, and this occurs, in the diffractive limit, for

$$\frac{\pi}{N_T} = \arccos\left(\frac{1 + l_D^2 q_I^2}{1 + l_D^2 q_{II}^2}\right). \tag{13}$$

In order to verify the validity of this relation, we proceed in the following way: for a given propagation length L we adjust the pump intensity I_0 in such a way that the system is just above threshold, then, starting from $N = 3$, we analyze the pattern for different feedback rotation angles $\Delta = 2\pi/N$ incrementing N by steps of 2. Looking at the far-field, we take as the transition point between the two unstable bands that for which a second ring develops inside the first one. Since the transition is not sharp and there are intermediate situations in which both wavelengths coexist, the N_T measured this way has an error bar ±2. Repeating the operation for various lengths L, we plot N_T vs. L. The experimental data (Fig. 18) are fitted with a line resulting from Eq. (13) with l_D as a free parameter. The best fit provides $l_D = 15.5$ μm. The inset of Fig. 18 shows the experimental far-field patterns at $L = 30$ cm and $N = 8$ and 9. In the N-odd case, since the pair of complex roots closest to the real axis provide a lower threshold at q_I, we have the same radius as for the even case, however the imaginary parts of the eigenvalues add a rotation in time, and hence the peaks are not resolved.

6. Conclusions

We have investigated the phenomena of pattern formation in a LCLV with feedback for various experimental configurations, and we have discussed the role of material nonlinearity and diffusion, longitudinal and transverse boundary condition and nonlocal interaction in determining the scale, the shape and, in some simple cases, the dynamics of the resulting structures. Most of the phenomena presented take place close to some instability threshold, and can therefore be accounted for by linear stability analysis of the underlying solutions.

Acknowledgements

Work partly supported by EEC contract n. CI1*CT93-0331.

References

[1] S.A. Akhmanov, M.A. Vorontsov, V. Yu. Ivanov, A.V. Larichev and N.I. Zheleznykh, J. Opt. Soc. Amer. B 9 (1992) 78.

[2] G. D'Alessandro and W.J. Firth, Phys. Rev. Lett. 66 (1990) 2597; G. D'Alessandro and W.J. Firth, Phys. Rev. A 46 (1992) 537.

[3] R. Macdonald and H.J. Eichler, Optim. Commun. 89 (1992) 289.

[4] M. Tamburrini, M. Bonavita, S. Wabnitz and E. Santamato, Optim. Lett. 18 (1993) 855.

[5] E. Pampaloni, S. Residori and F.T. Arecchi, Europhys. Lett. 24 (1993) 647.

[6] E. Pampaloni, P.L. Ramazza, S. Residori and F.T. Arecchi, Europhys. Lett. 25 (1994) 587.

[7] E. Pampaloni, P.L. Ramazza, S. Residori and F.T. Arecchi, Phys. Rev. Lett. 74 (1995) 258.

[8] F. Papoff, G. D'Alessandro, G.L. Oppo and W.J. Firth, Phys. Rev. A 48 (1993) 634.

[9] M.A. Vorontsov, M.E. Kirakosyan and A.V. Larichev, Soviet J. Quantum Electronics 21 (1991) 105.

[10] P.G. De Gennes, The Physics of Liquid Crystals (Oxford University Press, Oxford, 1974).

[11] G. D'Alessandro, E. Pampaloni, P.L. Ramazza, S. Residori and F.T. Arecchi, to be published in Phys. Rev. A (1995).

[12] D. Shechtman, I. Blech, D. Gratias and J.W. Cahn, Phys. Rev. Lett. 53 (1984) 1951; D. Levine and P.J. Steinhardt, Phys. Rev. Lett. 53 (1984) 2477; B. Christiansen, P. Alstrøm and M.T. Levinsen, Phys. Rev. Lett. 68 (1992) 2157; W.S. Edwards and S. Fauve, Phys. Rev. E 47 (1993) 788.

[13] B.A. Malomed, A.A. Nepomnyaschiĭ and M.I. Tribelskiĭ, Soviet Phys. JETP 69 (1989) 388; V.V. Beloshapkin, A.A. Chernikov, R.Z. Sagdeev and G.M. Zaslavsky, Phys. Lett. A 133 (1988) 395; A.A. Chernikov, R.Z. Sagdeev, D.A. Usikov and G.M. Zaslavsky, Comput. Math. Appl. 17 (1989) 17.

[14] H. Adachihara and H. Faid, J. Opt. Soc. Amer. B 10 (1993) 1242.